nature communications

Article

https://doi.org/10.1038/s41467-024-50560-1

# Reaching the efficiency limit of arbitrary polarization transformation with non-orthogonal metasurfaces

Received: 6 December 2023

Accepted: 15 July 2024

Published online: 06 August 2024

Check for updates

Yueyi Yuan[1], Kuang Zhang[1] ✉, Qun Wu[1], Shah Nawaz Burokur[2] ✉ & Patrice Genevet[3] ✉

Polarization transformation is at the foundation of modern applications in photonics and quantum optics. Notwithstanding their applicative interests, basic theoretical and experimental efforts are still needed to exploit the full potential of polarization optics. Here, we reveal that the coherent superposition of two non-orthogonal eigen-states of Jones matrix can improve drastically the efficiency of arbitrary polarization transformation with respect to classical orthogonal polarization optics. By exploiting metasurface with stacking and twisted configuration, we have implemented a powerful configuration, termed "non-orthogonal metasurfaces", and have experimentally demonstrated arbitrary input-output polarization modulation reaching nearly 100% transmission efficiency in a broadband and angle-insensitive manner. Additionally, we have proposed a routing methodology to project independent phase holograms with quadruplex circular polarization components. Our results outline a powerful paradigm to achieve extremely efficient polarization optics, and polarization multiplexing for communication and information encryption at microwave and optical frequencies.

On-demand polarization transformation is a momentous basis in various techno-spheres notably driven by applications, including polarimetric imaging, data storages, biosensing, and so forth[1–6]. Classical linear / circular to linear / circular polarization modulations have been sufficiently studied and applied in kinds of wireless related techniques[7–10]. With increasing requirements driven by various application scenarios, including intelligent augmented reality, and multi-dimensional vectoral imaging, the capability of achieving complex polarization modulations, i.e., arbitrary elliptical input polarization to elliptical output, is becoming ubiquitous both at optical and microwave frequencies[1,11,12]. Metamaterials and metasurfaces, providing flexibility and precise artificial modulation abilities of electromagnetic (EM) wave, have been extensively utilized to perform polarization manipulation[13,14]. As research progressing, the focus on arbitrary elliptical polarization conversion is gradually shifting from "How to realize" to "How to improve performance", including operation bandwidth, limited absorption losses with all-dielectric metasurfaces[15–17], multiple functionality integration through chiroptical responses and optical cryptography and so forth[18–24]. However, to go beyond these conceptual innovations and to succeed in developing industrially relevant applications, conversion efficiency - often disregarded in fundamental or conceptual studies- would be one of the most relevant factors for polarizing meta-devices. Although current approaches relying on conventional phase modulation schemes seem adequate to complete high-efficient regular linear/circular polarization transformations[12,25,26], they are not capable to achieve high efficiency of elliptical polarization modulations. From fundamental perspectives, we are in fact still lacking of quantitative and qualitative analysis methods to evaluate the arbitrary polarization performance.

[1]Department of Microwave Engineering, Harbin Institute of Technology, 150001 Harbin, China. [2]LEME, Univ Paris Nanterre, 92410 Ville d'Avray, France. [3]Physics department, Colorado School of Mines, 1523 Illinois, St, Golden, CO 80401, USA. ✉e-mail: zhangkuang@hit.edu.cn; sburokur@parisnanterre.fr; patrice.genevet@mines.edu

The physics describing the arbitrary polarization transformation efficiency depends on the matching degree between the targeted input-output combination and the equivalent complex 2 × 2 Jones matrix $\boldsymbol{J} = \begin{bmatrix} J_{xx} & J_{xy} \\ J_{yx} & J_{yy} \end{bmatrix} \in \mathbb{C}^{2\times 2}$ of the polarizing element in consideration[27,28]. From the point of view of spectrum theorem, eigen-formalisms (plural eigen-values $\boldsymbol{\kappa_{1,2}}$ and eigen-states $|\zeta_{1,2}\rangle$) comprehensively characterize the matching solutions of the system[29,30]. Here we define the degree of inhomogeneity $|\boldsymbol{\eta}| = |\langle\zeta_1|\zeta_2\rangle| \in [0,1]$ to describe the spatial parallelism between the eigen-state pair[28,29]. This parameter is often used to classify the Jones matrix and associated polarizing devices (Fig. 1A). When two eigen-states are orthogonal to each other ($|\boldsymbol{\eta}| = 0$, represented by antipodal Stokes vectors located on opposite sides of the Poincaré sphere and symmetric about the center), the corresponding Jones matrix is labelled as homogeneous[7]. This antipodal eigen-states configuration characterizes most classical polarizing devices and birefringent metamaterials, such as optical waveplates and polarizers, PB-phase meta-polarizers, Huygens-surfaces, and topology-optimized metasurfaces that separately carry *orthogonal* linear, circular, and elliptical polarized eigen-states[31–33]. For the other limit, $|\boldsymbol{\eta}| = 1$ characterizes the degenerated eigen-state pairs (Fig. 1A). This reveals the underlying principle of exceptional points (EPs) generation, which has attracted lots of attentions in quantum meta-optics, including plasmonic topological phase enabled by circling EP, observation of EPs through terahertz and acoustic metasurfaces[34–37]. These two extremal cases, orthogonality ($|\boldsymbol{\eta}| = 0$) and degeneration ($|\boldsymbol{\eta}| = 1$), only occupy a minority in the whole polarization space, and these extremal cases obviously limit the spatial freedom of eigen-state pairs for matching arbitrary input and output polarization. It becomes clear that the limitation of eigen-state pairs is the physical bottleneck for arbitrary polarization transformation efficiency. In contrast, the unexplored gap represented by $0 < |\boldsymbol{\eta}| < 1$, i.e. non-orthogonal cases, provides infinite quantity of polarization basis supporting inhomogeneous Jones matrix models[38]. Exploring this interesting intermediate regime, which requires working with slight absorption losses, offers extensive matching conditions to address various input output

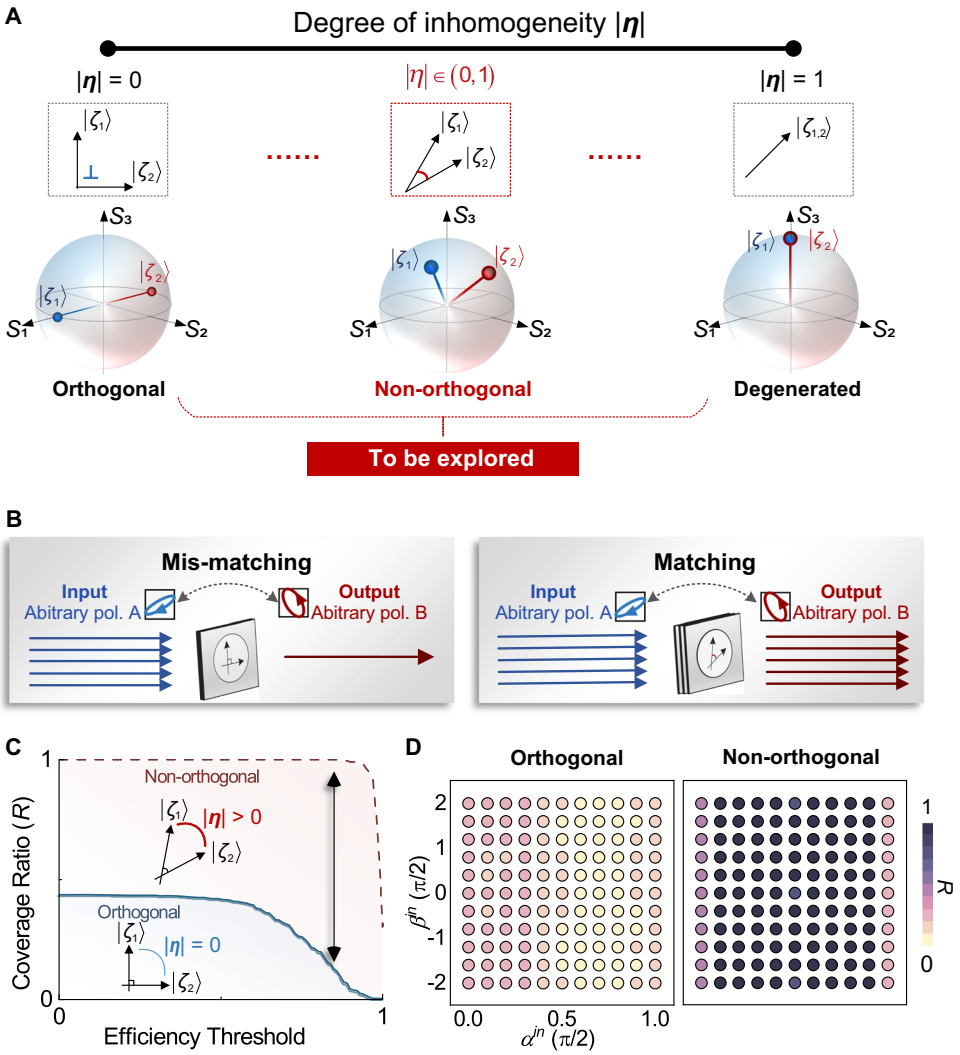


**Fig. 1 | Schematic description of the Jones matrix degree of homogeneity, ranging from orthogonal to non-orthogonal eigen-states, and associated advantages. A** Schematic catalog of inhomogeneity parameter $|\boldsymbol{\eta}|$ and corresponding eigen-states $|\zeta_i\rangle$ ($i = 1, 2$) labelled by the blue-red dot pairs on Poincaré sphere ($[S_1, S_2, S_3]$ represents the spheroidal coordinate), where the two extreme cases, namely orthogonal $|\boldsymbol{\eta}| = 0$[29–31] and fully degenerated $|\boldsymbol{\eta}| = 1$[32–35] are shown to only occupy a minority in the inhomogeneity set. Exploring the non-orthogonal gap with $0 < |\boldsymbol{\eta}| < 1$, we reveal that it contains new degree of freedoms for achieving arbitrary polarization modulation. **B** Mis-match case (left) indicating non-unitary transformation using orthogonal eigen-formalism, and (right) using non-orthogonal eigen-formalism, it is possible to match with almost unitary transformation arbitrary input elliptical polarization state (pol.) A to output pol. B. **C** Calculated coverage ratios $R$ of effective output states diagrams against efficiency threshold under a randomly selected input state. **D** Under arbitrary input states labelled by its Jones variables $\alpha^{in}$ and $\beta^{in}$, the coverage ratios $R$ of effective output states with orthogonal and non-orthogonal eigen-bases (efficiency threshold 0.9).

elliptical polarizations, theoretically guaranteeing extreme efficiency for arbitrary polarization conversions and manipulations.

Here we propose to study the transition from classical orthogonal eigen polarization base to non-orthogonal pairs, revealing a powerful mechanism for achieving near-unity efficiency for any arbitrary-to-arbitrary polarization transformation (Fig. 1B). We theoretically verify the orthogonality constrain on arbitrary polarization transformation, and then enhance corresponding efficiency to reach its fundamental limit close to unity through non-orthogonal eigen-formalism[28]. By analogy with optical systems composed of stacking and turning waveplates[39–41], we rely here on the mature fabrication technique for multilayered ultra-thin meta-devices[30,42–48], and implement a generic metasurface platform with stacking and twisted configuration to conduct non-orthogonal eigen-states, so-called non-orthogonal metasurface. With respect to existing literature, our approach both theoretically and experimentally proves that non-orthogonal metasurfaces can realize any desired input output polarization transformation with nearly 100% efficiency in a broadband and angle-insensitive manner. Moreover, the non-orthogonal metasurface scheme is capable of routing any one or more quadruplex circular polarization (CP) channels, meanwhile suppressing the others, and imposing independent holographic images into each channel separately.

## Results

### Operating principles and theoretical verifications

Here we firstly delve into the two-order non-Hermitian system, and express Jones matrix uniquely in terms of eigen-values and arbitrary eigen-states, according to spectrum expansion method[28,29]:

$$\boldsymbol{J}=\sum_{j=1}^{2}\sum_{i=1}^{2}\langle\zeta_i|\boldsymbol{J}|\xi_j\rangle|\zeta_i\rangle\langle\xi_j| \tag{1}$$

where $|\zeta_i\rangle\langle\zeta_i|$ denotes projection operator and $|\zeta_i\rangle\langle\xi_j|(i\neq j)$ represents the conversion operator, $|\zeta_i\rangle=\begin{bmatrix}\zeta_{ix}\\ \zeta_{iy}\end{bmatrix}$ $(i=1,\ 2)$ constitute the orthonormal basis of eigen-states and $|\xi_j\rangle$ $(j=1,2)$ denotes the corresponding reciprocal bi-orthogonal eigen-states that would satisfy $\langle\xi_i|\zeta_j\rangle=\begin{cases}1, i=j\\ 0, i\neq j\end{cases}$. Here we consider Jones matrix $\boldsymbol{J}$ containing four independent coefficients, with the eigen-values $\kappa_i=\frac{tr\boldsymbol{J}}{2}\pm\sqrt{(\frac{tr\boldsymbol{J}}{2})^2-\det\boldsymbol{J}}$ and eigen-states $|\zeta_i\rangle\propto\begin{bmatrix}J_{xx}-J_{yy}\pm\sqrt{(J_{xx}-J_{yy})^2+4J_{xy}J_{yx}}\\ J_{yx}\end{bmatrix}$ (normalized bi-orthogonal eigen-form $|\xi_j\rangle=\frac{e^{i\angle\eta}}{\sqrt{1-|\eta|^2}}|\zeta_i^{\perp}\rangle, i\neq j$), where $tr\boldsymbol{J}=J_{xx}+J_{yy}$ is the trace and $\det\boldsymbol{J}=J_{xx}J_{yy}-J_{xy}J_{yx}$ shows the determinant of the non-Hermitian matrix, superscript "$\perp$" presents the perpendicular vector. $\boldsymbol{\eta}$ is the complex inhomogeneity parameter, here $|\boldsymbol{\eta}|=|\langle\zeta_1|\zeta_2\rangle|\in[0,1]$ is the amplitude purposely introduced to denote the parallelism between two eigen-states, and $\angle\boldsymbol{\eta}$ presents the phase response. Consequently, we can derive non-Hermitian Jones matrices that sustains non-zero inhomogeneity in eigen-formalism:

$$\boldsymbol{J}=\boldsymbol{\kappa}_1\frac{e^{-i\angle\boldsymbol{\eta}}}{\sqrt{1-|\boldsymbol{\eta}|^2}}|\zeta_1\rangle\langle\zeta_2^{\perp}|+\boldsymbol{\kappa}_2\frac{e^{i\angle\boldsymbol{\eta}}}{\sqrt{1-|\boldsymbol{\eta}|^2}}|\zeta_2\rangle\langle\zeta_1^{\perp}| \tag{2}$$

When any arbitrary input polarization state $|\boldsymbol{E}^{in}\rangle$ is supposed to illuminate the polarizing element, the output polarization can be expressed by $|\boldsymbol{E}^{out}\rangle=\boldsymbol{J}|\boldsymbol{E}^{in}\rangle=\frac{\boldsymbol{\kappa}_1\boldsymbol{p}e^{-i\angle\boldsymbol{\eta}}}{\sqrt{1-|\boldsymbol{\eta}|^2}}|\zeta_1\rangle+\frac{\boldsymbol{\kappa}_2\boldsymbol{q}e^{i\angle\boldsymbol{\eta}}}{\sqrt{1-|\boldsymbol{\eta}|^2}}|\zeta_2\rangle$, where $\boldsymbol{p}=\langle\zeta_2^{\perp}|\boldsymbol{E}^{in}\rangle$ and $\boldsymbol{q}=\langle\zeta_1^{\perp}|\boldsymbol{E}^{in}\rangle$ denote the projections of input $|\boldsymbol{E}^{in}\rangle$ on two eigen-states $|\zeta_{1,2}^{\perp}\rangle$, respectively. Herein, transformation efficiency is measured by dividing the output light energy with preset polarization state relative to the input energy, comprising both polarization conversion efficiency and transmission efficiency, as denoted by:

$$T=\frac{\langle\boldsymbol{E}^{out}|\boldsymbol{E}^{out}\rangle}{\langle\boldsymbol{E}^{in}|\boldsymbol{E}^{in}\rangle}=\frac{|\boldsymbol{\kappa}_1|^2|\boldsymbol{p}|^2+|\boldsymbol{\kappa}_2|^2|\boldsymbol{q}|^2}{1-|\boldsymbol{\eta}|^2} \tag{3}$$

For conventional polarizing elements carrying orthogonal eigen-states ($|\boldsymbol{\eta}|=0$), the elliptical shape and declination angle of possible output polarizations are precisely dictated by corresponding eigen-values, which inherently contributes to the transformation efficiency. Although the efficiency can approach unity for specific input-output polarization scenarios highly matched by orthogonal eigen-states of homogeneous Jones matrices, these performances are only obtained for a minority of configurations[5]. Studying now the expression of the output signal obtained by passing through polarizing elements with non-orthogonal eigen-states ($|\boldsymbol{\eta}|>0$), the corresponding efficiency are not anymore determined only by the eigen-values $\boldsymbol{\kappa_{1,2}}$, but also depends on the degree of inhomogeneity $|\boldsymbol{\eta}|$. Such extra degree of freedom (DOF) $\boldsymbol{\eta}$ releases the orthogonal restriction of eigen-states, and provides tuning knob to theoretically approach efficiency limit for any arbitrary polarization transformation.

To quantitatively analyze the arbitrary polarization transformation efficiencies, Jones matrices with physically accessible complex coefficients are taken into consideration. By enforcing the strict eigen-state condition $|\boldsymbol{\eta}|=0$, Jones matrices are then arranged and classified into two groups: orthogonal and non-orthogonal libraries. We theoretically associate the transformation efficiency to any random collection of input and output states, which are chosen as to be representative to the average statistical distribution of polarization states on the Poincaré sphere (SI). We then set an efficiency threshold to evaluate the "effective output state" characterized by output efficiencies exceeding a preset threshold value. For any randomly selected input polarization state, we establish a concept of *coverage ratio* ($R$), depicting the ratio of effective outputs constrained by the efficiency threshold over the total number of all possible states in the polarization space (SI). Such coverage ratio $R$ is used to directly show the performance of polarization transformation under orthogonal and non-orthogonal eigen-formalisms (Fig. 1C). By increasing the efficiency threshold from 0 to 1 gradually, the coverage ratio of the output polarizations obtained from orthogonal eigen-states significantly decreases. Meanwhile, a strikingly different behavior is presented with non-orthogonal eigen bases, where $R$ is sustained close to unity with the efficiency threshold approaching 1. Such comparison indicates that by adopting the non-orthogonal eigen-state pairs of Jones matrices, the efficiency from any given input polarization to various output channels covering the entire Poincaré sphere can theoretically approach close to unity. Notably, reaching exactly the unity efficiency requires lossless cases for polarization transformations, however depending on the arbitrariness for polarization conversion, non-homogeneity is required and this cannot be achieved with pure lossless configuration (see Fig. S1 in SI). To compare the overall performances of both schemes, we study the polarization transformation scenarios for all possible input polarization states $|\boldsymbol{E}^{in}\rangle=\begin{bmatrix}\cos\alpha^{in}\\ \sin\alpha^{in}\cdot e^{i\beta^{in}}\end{bmatrix}$, where $\alpha^{in}\in[0,\frac{\pi}{2}]$ and $\beta^{in}\in[-\pi,\pi]$ denote the Jones variables. The choices of $\alpha^{in}$ and $\beta^{in}$ are uniformly sampled to cover the whole polarization space. For orthogonal eigen-states under variable input states (Fig. 1D), the coverage ratios of effective output states are around 0.2 with efficiency threshold of 0.9. Comparatively, through non-orthogonal eigen-states, the coverage ratios reach close to unity. These results encompass all possible input output polarization transformation situations, elucidating that even in the presence of slight losses, the non-orthogonality of the eigen-

https://doi.org/10.1038/s41467-024-50560-1

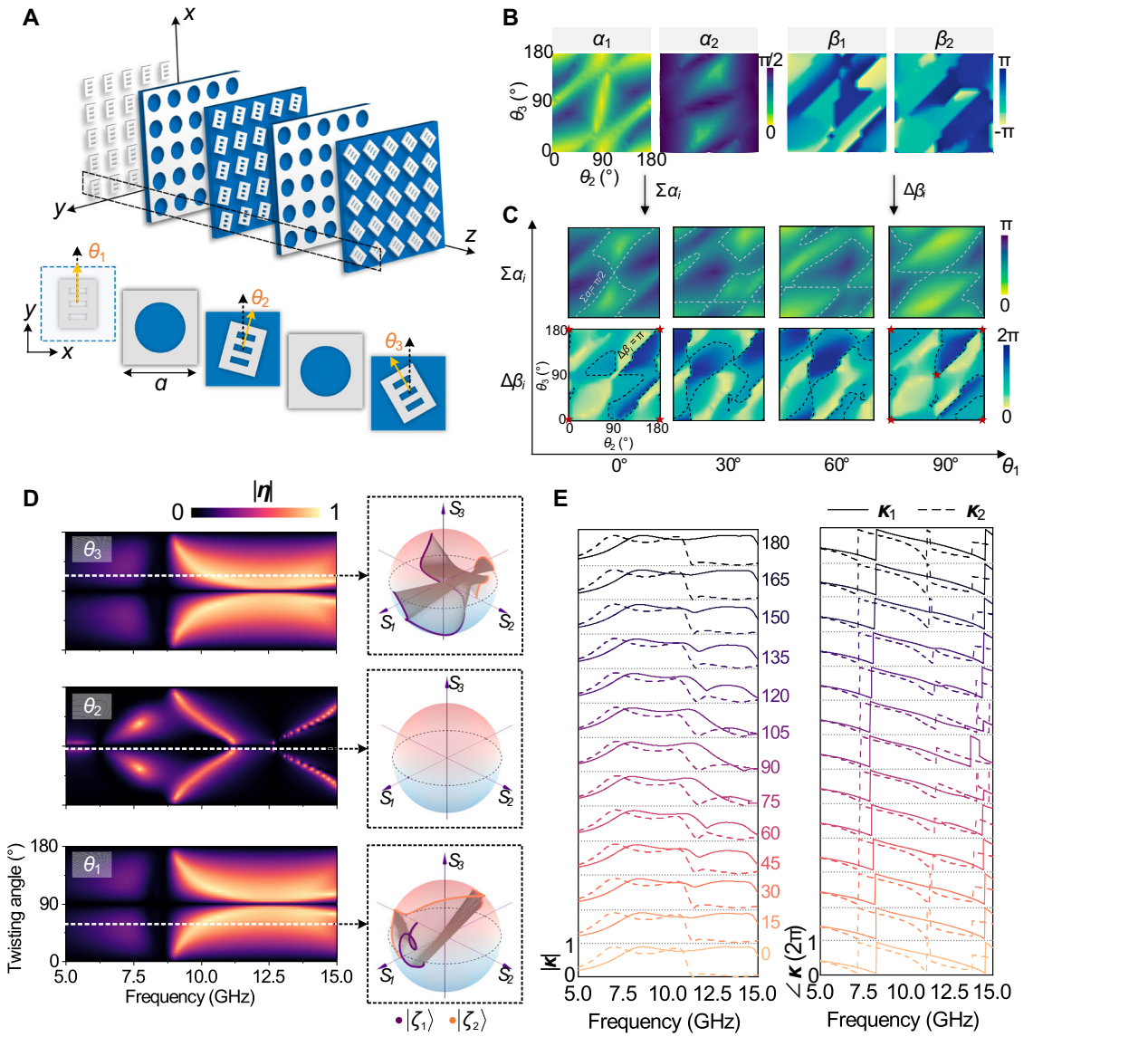


**Fig. 2 | Characteristics of non-orthogonal meta-atoms. A** Topological configuration of proposed non-orthogonal meta-atom with periodicity $a = 0.33\lambda_0$, distinct rotation angles of rectangular patches $\theta_n$ ($n = 1, 2, 3$) are the dominant factor for the non-orthogonal eigen-states implementation (other specific geometric parameters are explained in SI). **B** Independent profiles of Jones variables $\alpha_i$ and $\beta_i$ ($i = 1, 2$) in two eigen-states of meta-atom against variable $\theta_2$ and $\theta_3$ with fixed $\theta_1 = 0°$. **C** Evolution trends of $\Sigma\alpha_i = \alpha_1 + \alpha_2$ and $\Delta\beta_i = \beta_1 - \beta_2$ for meta-atom with variable $\theta_2$ and $\theta_3$ when $\theta_1 = 0°$, 30°, 60° and 90°, indicating the non-orthogonality between eigen-state pairs. Gray and black dotted lines separately present orthogonal requirements $\Sigma\alpha_i = \pi/2$ and $\Delta\beta_i = \pi$. Conventional orthogonal states occur at the overlapping point, indicated by the red stars. **D** Degree of inhomogeneity with separately variable $\theta_i$ as a function of the frequency, insets present the evolution of the trajectories of corresponding eigen-state pair on Poincaré sphere with frequency (5 GHz to 15 GHz) for the meta-atoms with $(\theta_1, \theta_2, \theta_3) = (60°, 0°, 0°)$, $(0°, 90°, 0°)$, and $(0°, 0°, 120°)$, respectively. **E** Amplitude and phase profiles of two non-orthogonal eigen-values of meta-atom with variable $\theta_1$ as the function of frequency, where gray dashed lines show the baselines of $|\boldsymbol{\kappa}| = 0$ and $\angle\boldsymbol{\kappa} = 0$.

states ($|\eta| > 0$) would support the complete eigen-modes in polarization space to match efficiently arbitrary input output polarization transformations.

## Meta-atom design for implementation strategies

The essential condition for implementing non-orthogonal eigen-state pairs is the symmetry-broken configurations along both tangential and normal directions, which simultaneously release constrains on the value of the coefficients in non-Hermitian Jones matrix[29,36]. Herein, we adopt a transmissive multilayered meta-atom (Fig. 2A) with non-resonant characteristics in the microwave band and consider realistic designs relevant for experimental proof-of-concept demonstration (SI). The $n^{th}$ birefringent patch with independent twisting angle $\theta_n$ ($n = 1, 2, 3$) is dominant factor for breaking in-plane and out-of-plane symmetries, where $n = 3$ is the minimum guarantee for full coverage of inhomogeneity parameter $|\boldsymbol{\eta}| \in [0,1]$ (derived and verified in SI). Notably, this stacking-twisted configuration for non-orthogonal eigen-formalism could be replaced by any other structure according to the operation wavelength of interest. For instance, the L-shaped element can be conducted in optical region (Note 9 in SI), and minimum layers for $|\boldsymbol{\eta}| \in [0,1]$ can be reduced down to only two layers when relying on in-plane complexity (Note 5 in SI).

To achieve formal description of this stacking and twisted configuration, we exploit wave matrix cascading model and calculate the non-Hermitian Jones matrix of the compound meta-atom[39] (SI). The

corresponding eigen-state pairs of such meta-atom, in Jones vector formalism, are expressed with distinct rotation of patches ($\theta_1$, $\theta_2$, $\theta_3$):

$$|\zeta_{1,2}\rangle = \begin{bmatrix} \zeta_{1x,2x} \\ \zeta_{1y,2y} \end{bmatrix} \propto \begin{bmatrix} -T_a \sum_{j=1}^{3} \cos(2\theta_j) - T_c \cos(2\theta_k) \pm P \\ -T_a \sum_{j=1}^{3} \sin(2\theta_j) + T_b \sum_{j=1}^{3} \sin(2\Delta\theta_j) - T_c \sin(2\theta_k) \end{bmatrix} \quad (4)$$

where $P = \sqrt{T_a^2 \sum_{j=1}^{3} \cos(4\theta_j) + (2T_a^2 + T_b^2) \sum_{j=1}^{3} \cos(2\Delta\theta_j) + T_c^2 \cos(4\theta_k) + 2T_a T_c \sum_{j=1}^{3} \cos 2(\theta_j + \theta_k)}$ is the decoupling factor for two eigen-states, $T_{a,b,c}$ represents coefficients as functions of scattering parameters of a single patch that vary with the area and aspect ratio, and $\Delta\theta_j$ shows the rotation offsets between distinct patches, including $\theta_1$ - $\theta_2$, $\theta_1$ - $\theta_3$, and $\theta_2$ - $\theta_3$, while $\theta_k = \theta_1 - \theta_2 + \theta_3$. To visualize the decoupling effects of stacked configuration on eigen-states, we track the evolution of eigen-state pairs as functions of twisting angles. Here, we adopt Jones variables $\alpha_i$ ($\alpha_i = \arctan(|\zeta_{iy}|/|\zeta_{ix}|), \in [0, \pi/2]$) and $\beta_i$ ($\beta_i = \angle\zeta_{iy} - \angle\zeta_{ix}, \in [-\pi, \pi]$) to present the relative trajectory of $i^{th}$ ($i = 1, 2$) eigen-state (Fig. 2B). When the top-layered patch is fixed to 0° and the other two patches are rotated from 0° to 180° separately, the profiles of $\alpha_1$ and $\alpha_2$ ($\beta_1$ and $\beta_2$) show completely different coverages and tendencies. This indicates that two eigen-states own distinct responses to the twisting configurations, and can be decoupled and co-modulated by changing $\theta_2$ and $\theta_3$. Increasing $\theta_1$ from 0° to 90°, evolution of $\Sigma\alpha_i$ and $\Delta\beta_i$ vary continuously (Fig. 2C), suggesting that the top-layered patch has an overall modulating effect on both eigen-states. Here the black dotted lines separately represent orthogonal conditions of $\Sigma\alpha_i = \pi/2$ and $\Delta\beta_i = \pi$[10], and the overlaps illustrating the orthogonal cases are labelled by red stars. We see that such twisting meta-atom would basically support the required non-orthogonal eigen-states except for the configurations with a high-level rotational symmetry. Then we evaluate the degree of inhomogeneity as a function of twisting angles within a broad bandwidth (Fig. 2D). Each separate $\theta_n$ changing from 0° to 180° is used to explore the full range $|\boldsymbol{\eta}| = [0, 1]$. It is seen that the mapping of $|\boldsymbol{\eta}|$ of meta-atoms with only rotating $\theta_1$ or $\theta_3$ are in same tendency, which is attributed to the reciprocal feature of configurations. Here, we illustrate the evolution of eigen-state pairs of some specific meta-atom configurations on Poincaré sphere, where the centroid (a)symmetry trajectories effectively prove the (non-)orthogonality eigen-performances. When a meta-atom has an in-plane rotationally symmetric pattern, the eigen-states are orthogonal and linear polarized, characteristic of widely reported birefringent meta-structures[29–31]. However, working with non-orthogonal modes, with adjustable amplitude and phase responses of eigen-values, can instead be used to define the desired output polarization performances, as shown in Eq. (3) (Fig. 2E). Non-resonant band-pass properties achieved through non-orthogonal eigen-values guarantee the high efficiency and stability of polarization conversion performances. By varying geometric configuration of patch elements, controllable amplitude diattenuation and phase retardance needed for arbitrary input output polarization matching can be obtained (SI). These results effectively prove that such meta-atom can support the entire polarization space to discretionarily tailor unrestricted eigen-formalism, paving solid foundation for implementing extremely-high efficient polarization transformations.

## Non-orthogonal metasurfaces for on-demand high-efficient polarization transformation

We experimentally verify the non-orthogonal metasurfaces, acting as polarization transformers with near unity efficiency performances. Here, we randomly select 8 input states expressed in Stokes parameters $|\boldsymbol{E}^{in}\rangle = \begin{bmatrix} S_1 \\ S_2 \\ S_3 \end{bmatrix} = \begin{bmatrix} \cos(2\alpha^{in}) \\ \sin(2\alpha^{in})\cos(\beta^{in}) \\ \sin(2\alpha^{in})\sin(\beta^{in}) \end{bmatrix} \begin{cases} \alpha^{in} \in [0, \frac{\pi}{2}] \\ \beta^{in} \in [-\pi, \pi] \end{cases}$, while under each input polarization, we preset 13 corresponding target output polarization states along the separate longitudinal path on Poincaré sphere. That is to say, 8 × 13 pairs of input-output polarization combinations in total are adopted to verify the arbitrariness and efficiency performances. Figure 3A displays an elliptical mapping of series of calculated (solid lines) and simulated (dotted lines) output polarization states under variable input states, where the gradual changes in elliptical geometries reveal the full coverage and arbitrariness of sampling in polarization space. Meanwhile, the agreement between simulated and ideal output states initially proves the feasibility of the non-orthogonal scheme. Besides, we also conducted multiple-input to single-output, single-input to multiple-output polarization conversions in SI, to verify the near-unity efficiency of arbitrary polarization conversion scheme.

To verify the practical polarization controlling performances, we fabricate a series of prototypes (13 individuals) to experimentally achieve desired high-efficient input-output arbitrary polarization transformations, as outlined by black dotted box in Fig. 3A (top row). The photograph of a fabricated meta-array sample is shown in Fig. 3B and the measurement setups and efficiency analyses for arbitrary input-output polarization conversions are specifically detailed in SI. Here, polarization transformation efficiencies ($T_{MS}$) of each 8 × 13 customized input output polarization conversion are calculated with Eq. (3) and displayed in Fig. 3C, where efficiencies are always reaching close to the unity. Meanwhile, the measured efficiency properties of all fabricated non-orthogonal metasurfaces are shown in the inset of Fig. 3C. The simulated average efficiency of the 13 samples reaches 96% (with maximum as 99%), and the measured average efficiency is over 92% (with maximum as 97%). Such deviation of measured efficiency is primarily caused by diffractions and noises in practical experimental setups. To validate the fidelity of output polarization responses, Stokes parameters ($S_1$, $S_2$ and $S_3$) of ideally preset, simulated, and measured output states, which are transformed from corresponding scattering parameters under horizontal linearly polarized illumination, are displayed in Fig. 3D. We adopt root-mean-square error (RMSE) qualifying the deviations from the pre-settings to quantitatively evaluate the polarization transformation effect. The simulated and measured RMSE of elliptical Stokes parameters are 0.04 and 0.05 ($S_1$), 0.03 and 0.08 ($S_2$), 0.05 and 0.05 ($S_3$), respectively. It is worth noting that the simulated output elliptical polarization states, constructed using full-wave metasurface modelling, are designed according to the geometrical parameters given by the corresponding fabricated samples. There exist some deviations between the simulated and measured Stokes parameters from the ideal pre-settings, especially for $S_1$ and $S_2$ of case 1 and 13 for circular polarizations, which are attributed to the finite geometric size of metasurface samples and the unavoidable interferences during measurement processes. Nevertheless, the barely undistorted polarization responses, measured experimentally, successfully validate the polarization modulation ability of the proposed non-orthogonal metasurfaces scheme.

Besides, we explored the bandwidth performance of proposed non-orthogonal eigen-formalism for arbitrary polarization conversions. We observed that the efficiency (transmittance) within the operating bandwidth ranges from 8 GHz to 12 GHz, i.e., with relative bandwidth of 40% of three representative samples ($11^{\#}$, $12^{\#}$, $13^{\#}$). When illuminated by linearly polarization incidence, measured transmittance profiles are displayed in Fig. 3E, and insets schematically present the configurations of three meta-devices and target input-output states. Transformation efficiency can be maintained approaching unity and peak values in measured profiles reaches to 95.1%, 94.2%, 95.6%, respectively. The error bars of efficiency profiles present the interference-induced noises and fluctuations within the measurement

https://doi.org/10.1038/s41467-024-50560-1

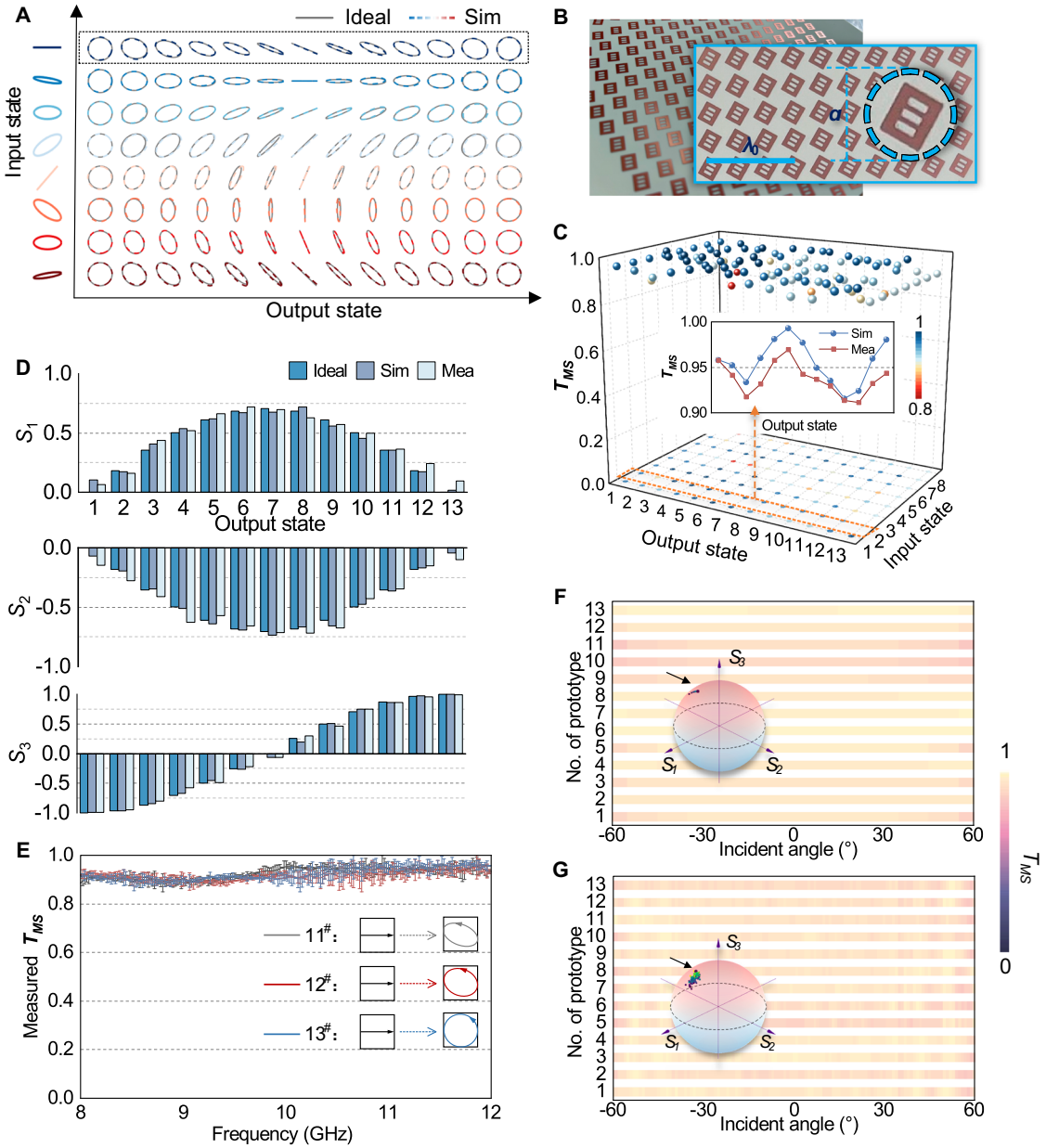


**Fig. 3 | Demonstrations of the non-orthogonal metasurfaces for high-efficient arbitrary polarization transformations. A** An elliptical mapping of variable ideal (solid line) and simulated (dotted line) output states under different preset input polarizations (8 × 13 pairs in total) to illustrate sampling arbitrariness. **B** Photograph of a fabricated sample, where the inset shows the locally enlarged meta-atom. **C** Simulated efficiencies of each input-output polarization transformation process, inset shows the comparison between simulated and measured efficiencies of fabricated non-orthogonal metasurface samples. **D** Calculated, simulated, and measured Stokes parameters ($S_1$, $S_2$, $S_3$) of output elliptical polarizations, which are transformed from scattering parameters under the horizontal linear polarization state. **E** Measured efficiency within the bandwidth of 8 GHz–12 GHz for the metasurface samples (11#, 12#, 13#). The error bars present the corresponding noisy fluctuations in the measurement processes, and the insets present the target input-output polarization conversions. **F** Simulated and (**G**) measured polarization transformation efficiencies ($T_{MS}$) of 13 representative prototype samples under oblique incidence from −60° to 60°, and the insets show simulated and measured output polarization states of the representative 11# sample under tilting incidence excited with linearly polarized beam, where the black dots pointed by arrows on Poincaré sphere denote the preset output polarization states.

processes. These efficiency performances indicate that the effective polarization conversion of fabricated meta-devices can be achieved within the entire bandwidth ranging from 8 GHz to 12 GHz. Note that our metasurfaces are composed of multiple metallic and dielectric layers, which bring unavoidable frequency dispersions, resulting in polarization variations within the operating bandwidth, as specifically analyzed in SI. Additionally, we have verified dependence properties of 13 prototypes under oblique incidence within −60° to 60° (Figs. 3F and 3G). The transmission performances can be maintained over 90% within the range of [-45°,45°] and slight degradations occur for incident angles from 45° to 60°. Figure 3G summarizes the corresponding measured efficiencies, indicating average efficiencies around 90% within tilting input angle 45°, and around 87% for incident angle 60°. To characterize the response of our system under oblique incidence excitation, we measure the response of the 11# metasurface (taken randomly as an example), excited with a horizontally polarized beam for incident angles ranging from -60° to 60°. The corresponding simulated and measured output polarizations are displayed on Poincaré sphere (inset of Figs. 3F and 3G), indicating only slight deviation from the target state with fluctuation RMSEs in Stokes parameters of

0.03 and 0.07 ($S_1$), 0.13 and 0.16 ($S_2$), 0.07 and 0.08 ($S_3$), respectively. These experiments verify that our non-orthogonal metasurfaces designed for arbitrary polarization conversions own angle-insensitivity responses for non-normal incidence within [−45°, 45°].

### Unrestricted eigen-states enabled $C_4^i$ gating of circular polarization channels and independent hologram manipulation

To demonstrate the extremely versatility achievable with non-orthogonal metasurfaces, we take an additional step further by routing multiple input signals towards multiple output ports with selection and modulation effects. Here we experimentally take circular polarization base as demonstration, to conduct $\boldsymbol{C}_4^i$ gating effects on all four CP channels, namely L-L, R-L, L-R and R-R (left-handed circularly polarized (LHCP) output - LHCP input, right-handed circularly polarized (RHCP) output - LHCP input, LHCP output - RHCP input, and RHCP output - RHCP input) channels. Any non-orthogonal pair of eigen-states $|\zeta_{1,2}\rangle$ can be decomposed into LHCP state $|L\rangle$ and RHCP state $|R\rangle$ with two distinct coefficients. According to the inherent steadiness associated to eigen polarization states passing through the analogue-chiral non-Hermitian element $\boldsymbol{J}$, the transmission process can be depicted with circular polarization base. We define and derive CP transmission complex coefficient $\boldsymbol{F}_{uv}$ (the subscript $u$ and $v$ represents output and input state as LHCP or RHCP) as detailed in SI. Therefore, we can deliberately select $i$ ($i = 1, 2, 3, 4$) and suppress the other (4 - $i$) channels by manipulating amplitude responses $\boldsymbol{F}_{uv}$ approaching 1 or 0, defined as $\boldsymbol{C}_4^i$ routing of CP channels, as schematically illustrated by shining on or off bulbs in Fig. 4A. To give an insight into the relationship between the routed channels and the inhomogeneity of the two eigen-polarizations, we set selected threshold as $|\boldsymbol{F}| > 0.7$ and suppressed threshold as $|\boldsymbol{F}| < 0.1$. Considering arbitrary inhomogeneous Jones matrices with $\boldsymbol{F}_{uv}$ satisfying the threshold condition of $\boldsymbol{C}_4^i$ routing ($i = 1, 2, 3, 4$), respectively, the distributions of theoretically calculated eigen-states are displayed on Poincaré sphere in Fig. 4A. For $\boldsymbol{C}_4^1$ gating effect of L-L channel with coefficient threshold $|F_{LL}| \to 1$, $|F_{RL}| \to 0$, $|F_{LR}| \to 0$, $|F_{RR}| \to 0$, the eigenvectors of satisfactory Jones matrices are distributed around north and south poles, indicating that such single-channel routing can be guaranteed by quasi circular eigen-polarizations. With the number of selected channels increasing, the distributions of eigen-states on Poincaré sphere get widen. Especially for $\boldsymbol{C}_4^4$ effect, the corresponding eigen-states can uniformly distribute almost full sphere, further demonstrating the high degree of non-orthogonality. Notably, the routing effects on CP channels only involve amplitude threshold of $\boldsymbol{F}_{uv}$, without any limitations on phase response of $\boldsymbol{F}_{uv}$. Thus, based on the degree of freedom of non-orthogonality between eigen-states, we can additionally impose premeditated phase distributions in gated channel $\boldsymbol{F}_{uv}$ to fulfill independent holographic images.

To demonstrate the phase modulation, independent hologram images of characters "1", "2", "3", "4" are imposed to L-L, R-L, L-R and R-R channels, respectively. For the simplicity of illustration, we exhibit four representative analogue-chiral metasurfaces for $\boldsymbol{C}_4^i$ routing and one fabricated sample is displayed in Fig. 4B. Under normal illumination of LHCP or RHCP beams propagating along +z-axis, measured energy intensities (Fig. 4C) of image projecting properties at pre-set plane with $z = 5\lambda_0$ indicate successfully produced CP transmitting channel gating with holographic manipulation. Despite the rough quality of the holographic projections (detailed analyzed in SI), the gating effect using phase-only metasurfaces can be validated. For more experimental details, the readers can refer to the SI. To evaluate the performance of holographic projection, we calculate the efficiency $\boldsymbol{T}_{\boldsymbol{ML}} = \frac{\sum_{x,y}|\boldsymbol{E}_o^{L/R}(x,y)||\boldsymbol{E}_o^{L/R}(x,y)\rangle}{\sum_{x,y}|\boldsymbol{E}_i^{L/R}(x,y)||\boldsymbol{E}_i^{L/R}(x,y)\rangle}$ in each separate CP channel of the fabricated sample, where $|\boldsymbol{E}_o^{L/R}(x,y)\rangle$ and $|\boldsymbol{E}_i^{L/R}(x,y)\rangle$ express respectively the output and the input electric fields selected as $|L\rangle$ or $|R\rangle$ state at specific coordination $(x, y)$ in measured plane. Figure 4D displays the measured $\boldsymbol{T}_{\boldsymbol{ML}}$ in each CP channel of four fabricated samples with $\boldsymbol{C}_4^i$ effect. The effective energy in gated CP channel(s) are obviously higher than the suppressed channel(s), attributing to the inhomogeneity degree supported in non-orthogonal metasurfaces. In addition, when just one channel is selected (e.g. $\boldsymbol{C}_4^1$ for L-L channel), the measured efficiency reaches 83%, while efficiencies in other three channels are 11% (R-L), 22% (L-R), 7% (R-R), respectively. When more than one channel are selected (i.e. $\boldsymbol{C}_4^i, i>1$), the efficiencies in distinct selected channels are obviously reduced. This is due to multiple ports working simultaneously, and evenly distributed energy in separate selected channels guarantees the quality of multiple output holographic projections.

Furthermore, we adopt a correlation coefficient $\rho_0$ between the measured and calculated images to characterize the hologram quality, as calculated by $\rho_0(\boldsymbol{I}_{ideal}, \boldsymbol{I}_{mea}) = \frac{COV(\boldsymbol{I}_{ideal}, \boldsymbol{I}_{mea})}{\sqrt{D(\boldsymbol{I}_{ideal})}\sqrt{D(\boldsymbol{I}_{mea})}}$[18], where $COV$ ($\boldsymbol{I}_{ideal}$, $\boldsymbol{I}_{mea}$) is the covariance of theoretically calculated hologram intensity $\boldsymbol{I}_{ideal}$ and measured energy intensity $\boldsymbol{I}_{mea}$, and $D(\boldsymbol{I}_{ideal})$ and $D(\boldsymbol{I}_{mea})$ shows the variances of corresponding intensities, respectively. The measured correlation coefficient $\rho_0$ within the bandwidth of 9 GHz – 11 GHz are illustrated in Fig. 4E. The contrast ratio of $\rho_0$ profiles in the selected and suppressed channels verifies the proposed CP routing scheme. The holographic imaging quality reaches its optimal value around the center operating frequency at 10 GHz, and accordingly degraded when deviating from nominal operating frequency. Nevertheless, the holographic image rendering is clearly produced at other frequency points (SI). This imaging resolution limit can be further optimized by neural network-based amplitude-phase holographic algorithms in future research. We have also analyzed the crosstalk between different CP channels. Correlation coefficient $\rho_{mn}$ is adopted to evaluate the interference between measured holographic intensities in selected $m^{th}$ and $n^{th}$ channels, as expressed by $\rho_{mn}(\boldsymbol{I}_m, \boldsymbol{I}_n) = \frac{COV(\boldsymbol{I}_m, \boldsymbol{I}_n)}{\sqrt{D(\boldsymbol{I}_m)}\sqrt{D(\boldsymbol{I}_n)}}$[18], where detailed calculations are expressed in SI. Measured $\rho_{mn}$ of these four metasurface samples at 10 GHz are illustrated in Fig. 4F. The gray area indicates invalid value under such conditions. For metasurface with $\boldsymbol{C}_4^1$ gating of L-L channel, the cross-talks produced by imaging "1" in R-L, L-R and R-R channels are 6%, 38.5% and 36.6%, respectively. The high cross-talks in L-R and R-R channels are due to the phase errors from discretization and amplitude sacrifices of meta-atoms, which can be further suppressed through configuration optimizations to provide eigen-formalism with higher matching degree. Meanwhile, the other cross-talks in multiple channel selections are all lower than 10%. Hence, our strategy provides a direct and convenient method for channels expansion and modulation in optical and wireless communication systems.

## Discussion

To summarize, we have proposed leveraging new framework for realizing arbitrary polarization transformations with near unity efficiency, essentially relying on the non-orthogonality of eigen-state pairs of non-Hermitian Jones matrices. Using multilayered metasurfaces to relax the orthogonality between polarization eigen-states, we provide an additional DOF of inhomogeneity parameter, which is used to achieve close to unity arbitrary polarization transformation efficiency in a broadband and angle-insensitive manner. We further extend the light modulation capabilities of our scheme to enable gating and independent wavefront modulation in quadplex transmitting channels. With respect to the existing polarizing devices relying on orthogonal eigen-bases, non-orthogonal metasurfaces provide exciting application opportunities, including but not limited to photonic polarizing devices, polarimetric imaging, polarization multiplexing in communication systems.

https://doi.org/10.1038/s41467-024-50560-1

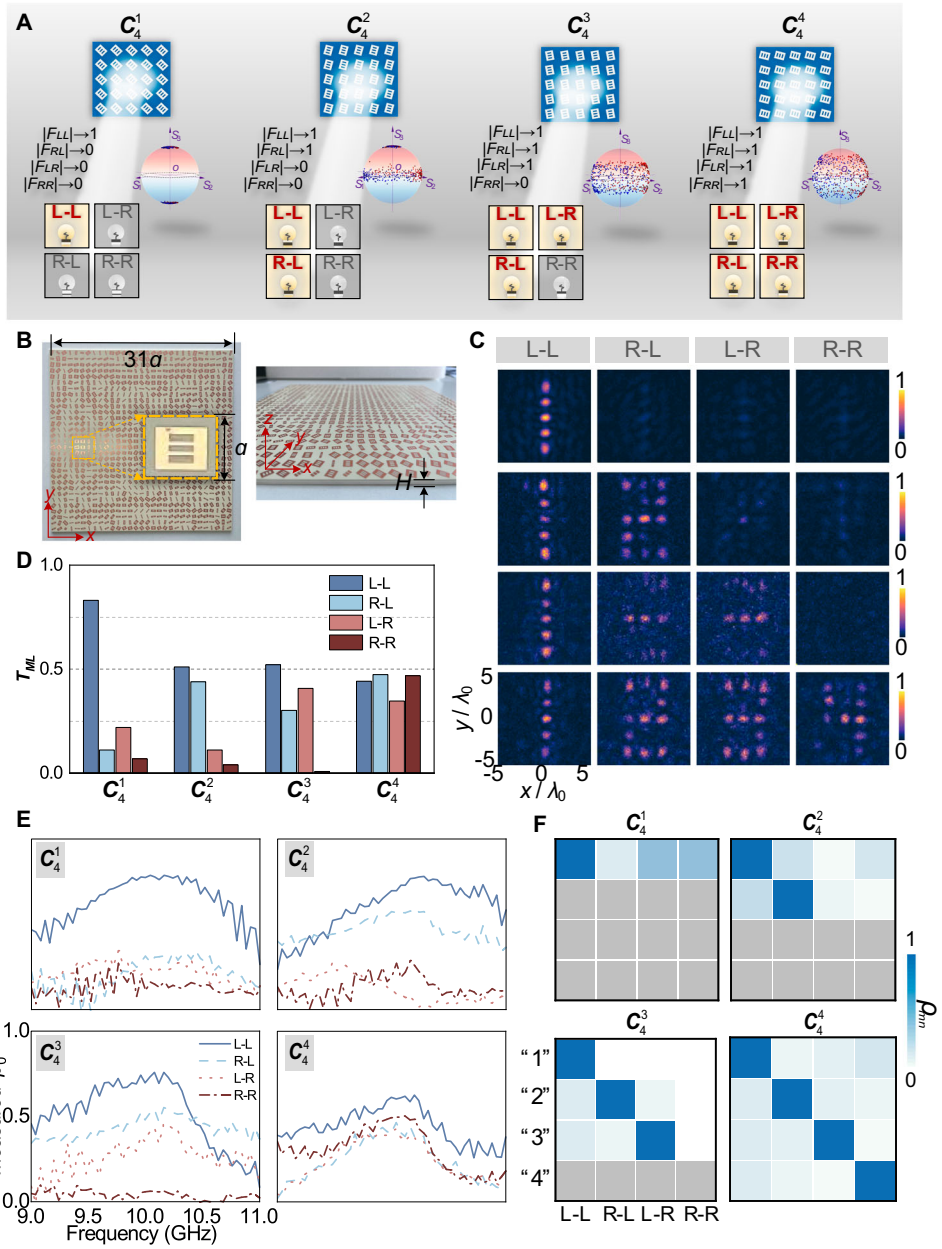


**Fig. 4 | $C_4^i$ gating of CP channels and independent hologram manipulation.** (**A**) Schematic of the proposed mechanism for different $C_4^i$ ($i = 1, 2, 3, 4$) gating effects. The schematics representing on and off light bulbs are used to illustrate the gated and suppressed channels. Insets also display the corresponding distributions of theoretically calculated eigen-state pairs on the Poincaré spheres. **B** Photograph of fabricated sample for $C_4^1$ gating for L-L channel, where $H$ denote the total thickness (about $0.15\lambda_0$) of the sample. **C** Measured energy intensity in $xy$ plane with $z = 5\lambda_0$ of four representative non-orthogonal metasurfaces for $C_4^1$ gating with hologram image "1" in L-L channel, $C_4^2$ gating with "1" in L-L channel and "2" in R-L channel, $C_4^3$ gating with "1", "2", "3" in L-L, R-L and L-R channel, $C_4^4$ gating with "1", "2", "3", "4" in all four channels, respectively. **D** Measured efficiencies in all CP channels of four fabricated samples. **E** Measured correlation coefficient $\rho_0$ of four representative samples within the bandwidth. **F** Measured $\rho_{mn}$ for cross-talk characterization at 10 GHz.

## Methods

There exist methods for sample fabrication and the experimental setups, which have been specifically discussed in Note 7 of Supplementary Information.

## Data availability

The main data supporting the findings of this study are available within the article and its Supplementary Information.

## References

1. Rubin, N. A. et al. Matrix Fourier optics enables a compact full-Stokes polarization camera. *Science* **365**, eaax1839 (2019).
2. Yesilkoy, F. et al. Ultrasensitive hyperspectral imaging and biodetection enabled by dielectric metasurfaces. *Nat. Photonics* **13**, 390–396 (2019).
3. Huang, C. X., Zhang, J., Cheng, Q. & Cui, T. J. Polarization modulation for wireless communications based on metasurfaces. *Adv. Funct. Mater.* **31**, 2103379 (2021).
4. Zang, H., Xi, Z., Zhang, Z., Lu, Y. & Wang, P. Ultrasensitive and long-range transverse displacement metrology with polarization-encoded metasurface. *Sci. Adv.* **8**, eadd1973 (2022).
5. Hong, J. et al. Nonlocal metasurface for circularly polarized light detection. *Optica* **10**, 134–141 (2023).

6. Song, J.-H., van de Groep, J., Kim, S. J. & Brongersma, M. L. Non-local metasurfaces for spectrally decoupled wavefront manipulation and eye tracking. *Nat. Nanotechnol.* **16**, 1224–1230 (2021).
7. Damask J. N. *Polarization optics in telecommunications*. (Springer Science & Business Media, 2004).
8. Zhang, X., Liu, Y., Han, J., Kivshar, Y. & Song, Q. Chiral emission from resonant metasurfaces. *Science* **377**, 1215–1218 (2022).
9. Shurcliff W. A. *Polarized Light*. Production and Use (Harvard University Press, 2013).
10. Lou, B., Wang, B., Rodríguez, J. A., Cappelli, M. & Fan, S. Tunable guided resonance in twisted bilayer photonic crystal. *Sci. Adv.* **8**, eadd4339 (2022).
11. Yin, K. et al. Advanced liquid crystal devices for augmented reality and virtual reality displays: principles and applications. *Light.: Sci. Appl.* **11**, 161 (2022).
12. Song, Q. et al. Ptychography retrieval of fully polarized holograms from geometric-phase metasurfaces. *Nat. Commun.* **11**, 2651 (2020).
13. So, S., Mun, J., Park, J. & Rho, J. Revisiting the Design Strategies for Metasurfaces: Fundamental Physics, Optimization, and Beyond. *Adv. Mater.* **35**, 2206399 (2023).
14. Yang, Y. et al. Integrated metasurfaces for re-envisioning a near-future disruptive optical platform. *Light.: Sci. Appl.* **12**, 152 (2023).
15. Ren, H. et al. An achromatic metafiber for focusing and imaging across the entire telecommunication range. *Nat. Commun.* **13**, 4183 (2022).
16. Biswas, S., Grajower, M. Y., Watanabe, K., Taniguchi, T. & Atwater, H. A. Broadband electro-optic polarization conversion with atomically thin black phosphorus. *Science* **374**, 448–453 (2021).
17. Song, Q. et al. Bandwidth-unlimited polarization-maintaining metasurfaces. *Sci. Adv.* **7**, eabe1112 (2021).
18. Guo, X. et al. Stokes meta-hologram toward optical cryptography. *Nat. Commun.* **13**, 6687 (2022).
19. Zhang, F. et al. Meta-optics empowered vector visual cryptography for high security and rapid decryption. *Nat. Commun.* **14**, 1946 (2023).
20. Xiong, B. et al. Breaking the limitation of polarization multiplexing in optical metasurfaces with engineered noise. *Science* **379**, 294–299 (2023).
21. Devlin, R. C., Ambrosio, A., Rubin, N. A., Mueller, J. P. B. & Capasso, F. Arbitrary spin-to-orbital angular momentum conversion of light. *Science* **358**, 896–901 (2017).
22. Shi, T. et al. Planar chiral metasurfaces with maximal and tunable chiroptical response driven by bound states in the continuum. *Nat. Commun.* **13**, 4111 (2022).
23. Ren, H. et al. Complex-amplitude metasurface-based orbital angular momentum holography in momentum space. *Nat. Nanotechnol.* **15**, 948–955 (2020).
24. Malek, S. C., Overvig, A. C., Alù, A. & Yu, N. Multifunctional resonant wavefront-shaping meta-optics based on multilayer and multi-perturbation nonlocal metasurfaces. *Light.: Sci. Appl.* **11**, 246 (2022).
25. Grady, N. K. et al. Terahertz Metamaterials for Linear Polarization Conversion and Anomalous Refraction. *Science* **340**, 1304–1307 (2013).
26. Momosaki, R. et al. Theoretical determination of biaxial anisotropy suitable for reducing incident angle dependence of a high-efficiency polarization grating. *J. Optical Soc. Am. B* **39**, 1964–1971 (2022).
27. Rubin, N. A., Shi, Z. & Capasso, F. Polarization in diffractive optics and metasurfaces. *Adv. Opt. Photonics* **13**, 836–970 (2021).
28. Lu, S.-Y. & Chipman, R. A. Homogeneous and inhomogeneous Jones matrices. *J. Optical Soc. Am. A* **11**, 766–773 (1994).
29. Tiberiu, T. Generalized observables in polarization optics. *J. Phys. A: Math. Gen.* **36**, 9577 (2003).
30. Cerjan, A. & Fan, S. Achieving Arbitrary Control over Pairs of Polarization States Using Complex Birefringent Metamaterials. *Phys. Rev. Lett.* **118**, 253902 (2017).
31. Shi, Z. et al. Continuous angle-tunable birefringence with freeform metasurfaces for arbitrary polarization conversion. *Sci. Adv.* **6**, eaba3367 (2020).
32. Mueller, J. P. B., Rubin, N. A., Devlin, R. C., Groever, B. & Capasso, F. Metasurface Polarization Optics: Independent Phase Control of Arbitrary Orthogonal States of Polarization. *Phys. Rev. Lett.* **118**, 113901 (2017).
33. Selvanayagam, M. & Eleftheriades, G. V. Polarization Control Using Tensor Huygens Surfaces. *IEEE Trans. Antennas Propag.* **62**, 6155–6168 (2014).
34. Song, Q., Odeh, M., Zúñiga-Pérez, J., Kanté, B. & Genevet, P. Plasmonic topological metasurface by encircling an exceptional point. *Science* **373**, 1133–1137 (2021).
35. Xu, H., Mason, D., Jiang, L. & Harris, J. G. E. Topological energy transfer in an optomechanical system with exceptional points. *Nature* **537**, 80–83 (2016).
36. Wang, X., Fang, X., Mao, D., Jing, Y. & Li, Y. Extremely Asymmetrical Acoustic Metasurface Mirror at the Exceptional Point. *Phys. Rev. Lett.* **123**, 214302 (2019).
37. Lawrence, M. et al. Manifestation of $PT$ Symmetry Breaking in Polarization Space with Terahertz Metasurfaces. *Phys. Rev. Lett.* **113**, 093901 (2014).
38. Gutiérrez-Vega, J. C. The field of values of Jones matrices: classification and special cases. *Proc. R. Soc. A* **476**, 20200361 (2020).
39. Tudor, T. Nonorthogonal polarizers: a polar analysis. *Opt. Lett.* **39**, 1537–1540 (2014).
40. Sakamoto, M. et al. Polarized beam steering using multiply-cascaded rotating polarization gratings. *Appl. Opt.* **60**, 2062–2068 (2021).
41. Ranjbar, A. & Grbic, A. Analysis and synthesis of cascaded metasurfaces using wave matrices. *Phys. Rev. B* **95**, 205114 (2017).
42. Wang, E. W., Phan, T., Yu, S.-J., Dhuey, S. & Fan, J. A. Dynamic circular birefringence response with fractured geometric phase metasurface systems. *Proc. Natl Acad. Sci. USA* **119**, e2122085119 (2022).
43. Li, Z. et al. Inverse Design of Few-Layer Metasurfaces Empowered by the Matrix Theory of Multilayer Optics. *Phys. Rev. Appl.* **17**, 024008 (2022).
44. Zhao, Y., Belkin, M. A. & Alù, A. Twisted optical metamaterials for planarized ultrathin broadband circular polarizers. *Nat. Commun.* **3**, 870 (2012).
45. Khaliji, K., Martín-Moreno, L., Avouris, P., Oh, S.-H. & Low, T. Twisted Two-Dimensional Material Stacks for Polarization Optics. *Phys. Rev. Lett.* **128**, 193902 (2022).
46. Hu, G., Wang, M., Mazor, Y., Qiu, C.-W. & Alù, A. Tailoring Light with Layered and Moiré Metasurfaces. *Trends Chem.* **3**, 342–358 (2021).
47. Han, Z., Wang, F., Sun, J., Wang, X. & Tang, Z. Recent Advances in Ultrathin Chiral Metasurfaces by Twisted Stacking. *Adv. Mater.* **35**, 2206141 (2023).
48. Liu, N., Liu, H., Zhu, S. & Giessen, H. Stereometamaterials. *Nat. Photonics* **3**, 157–162 (2009).


## Acknowledgements

Y.Y. acknowledges the support from National Science Foundation of China (No. 62301193) and Young Elite Scientists Sponsorship Program by CAST (2023QNRC001). K.Z. acknowledges the support from National Science Foundation of China (U23B2014, 62171165) and the Fundamental Research Funds for the Central Universities (HIT.OCEF.2021011). P.G. acknowledges financial support by the French National Research Agency ANR Project DILEMMA (ANR-20-CE09-0027) and from the European Innovation Council (EIC) project Twisted Nano (under the grant agreement number Pathfinder Open 2021- 101046424).

## Author contributions

K.Z., S.N.B. and P.G. conceived the idea. Y.Y. and K.Z. conducted the numerical simulations and theoretical analysis. S.N.B. and Y.Y. conducted the experiments. Y.Y., K.Z., Q.W., S.N.B. and P.G. wrote the manuscript.

## Competing interests

The authors declare no competing interests.

## Additional information

**Supplementary information** The online version contains supplementary material available at https://doi.org/10.1038/s41467-024-50560-1.

**Correspondence** and requests for materials should be addressed to Kuang Zhang, Shah Nawaz Burokur or Patrice Genevet.

**Peer review information** *Nature Communications* thanks Tie Jun Cui, Marcus Ossiander, Junsuk Rho and Jian Wei You for their contribution to the peer review of this work. A peer review file is available.